



OPEN

# Correlative Tomography

T. L. Burnett<sup>1,2</sup>, S. A. McDonald<sup>1,3</sup>, A. Gholinia<sup>1</sup>, R. Geurts<sup>2</sup>, M. Janus<sup>2</sup>, T. Slater<sup>1</sup>, S. J. Haigh<sup>1</sup>, C. Ornek<sup>1</sup>, F. Almuili<sup>1</sup>, D. L. Engelberg<sup>1</sup>, G. E. Thompson<sup>1</sup> & P. J. Withers<sup>1,3</sup>

SUBJECT AREAS:

METALS AND ALLOYS

IMAGING TECHNIQUES

Received

5 February 2014

Accepted

31 March 2014

Published

16 April 2014

Correspondence and requests for materials should be addressed to P.J.W. (Philip. Withers@manchester.ac.uk)

<sup>1</sup>School of Materials, University of Manchester, Manchester, M13 9PL, UK, <sup>2</sup>FEI Company, Achtseweg Noord 5, Bldg 5651 GG, Eindhoven, The Netherlands, <sup>3</sup>BP International Centre for Advanced Materials, School of Materials, University of Manchester, Manchester, M13 9PL, UK.

Increasingly researchers are looking to bring together perspectives across multiple scales, or to combine insights from different techniques, for the same region of interest. To this end, correlative microscopy has already yielded substantial new insights in two dimensions (2D). Here we develop correlative tomography where the correlative task is somewhat more challenging because the volume of interest is typically hidden beneath the sample surface. We have threaded together x-ray computed tomography, serial section FIB-SEM tomography, electron backscatter diffraction and finally TEM elemental analysis all for the same 3D region. This has allowed observation of the competition between pitting corrosion and intergranular corrosion at multiple scales revealing the structural hierarchy, crystallography and chemistry of veiled corrosion pits in stainless steel. With automated correlative workflows and co-visualization of the multi-scale or multi-modal datasets the technique promises to provide insights across biological, geological and materials science that are impossible using either individual or multiple uncorrelated techniques.

The spatial registration of two or more imaging modalities, often termed correlative microscopy, allows different types of information, or insights at different scales, to be brought to bear on the same region of interest. For example, combining fluorescence microscopy and electron microscopy is becoming increasingly popular in biology for associating the location of fluorescent markers with high resolution imaging techniques<sup>1</sup>. This approach has been aided by automated workflows that make the registration of the same area recorded by multiple instruments relatively straightforward technically. However, many important events occur well beneath the surface and in three dimensions (3D). In this paper we propose ‘*correlative tomography*’, whereby multiple techniques are brought together for a three dimensional volume of interest and present a simple workflow by which this can be achieved in practice.

Many features require 3D characterization, for example, to establish, quantify and model the interconnectivity of networks e.g. blood vessels, pore channels in rocks, fibres in composites, or morphologies, e.g. of porosity, second phase particles or fracture paths<sup>2–6</sup>. In this respect X-ray computed tomography (CT) has proven itself to be a powerful characterization technique for the non-destructive imaging of medical, biological and materials science specimens at the millimetre to micron scale<sup>2</sup>. In some cases multiple 3D imaging techniques have been combined. For example Positron Emission Tomography (PET) and X-ray CT are routinely combined in medical imaging<sup>7</sup> and X-ray CT and serial sectioning of the same volume has been carried out<sup>8–10</sup>. To bridge a range of scales multiple techniques have been used to quantify the size of pores etc., but predominantly in an uncorrelated statistical manner<sup>11–13</sup>. There are a few instances where a degree of spatial correlation has been employed to match, subsequently produced, destructive 2D cross sections to virtual sections identified by non-destructive 3D imaging<sup>14–18</sup>. However, new insights can be gained by employing correlative tomography whereby a 3D region of interest is identified for sequential investigation at a finer scale and/or by a complementary modality.

In this paper, we introduce the concept of correlative tomography. This requires the spatial registration of multiple techniques on the exact same region of interest in 3D with each 3D dataset steering the location and choice of the next volume to be analysed. The power of the method and the necessary workflow needed to locate and co-register the 3D information is exemplified in this paper through a study of the competition between pitting and intergranular corrosion in a sensitised austenitic stainless steel. The corrosion of stainless steel components in chloride-containing environments and, specifically, the rate and manner in which the localized corrosion progresses is critical from a structural integrity viewpoint in estimating the safe lifetime of components across a range of applications in the energy industry especially in nuclear and oil & gas plants<sup>19</sup>. Finally, the wider applications and possibilities of correlative tomography in accessing multiple scales and time dependent phenomena in 3D are considered.



## Results

**Workflow for 3D correlative tomography.** Automated workflows now exist for the spatial registration of regions of interest in 2D for correlative microscopy<sup>20</sup>. While conceptually the same, the task of correlating submerged volumes in 3D is somewhat more challenging. At the present time our workflow for the co-registration of successive techniques applied at increasing magnifications to focus on the same submerged volume of interest is a manual one (see Fig. 1 and S1), though considerable potential exists for automated workflows in the future. Initially, a single corrosion pit has been selected from many observed in the large field of view provided by non-destructive medium resolution X-ray CT (A1). Despite being concealed below the surface by its lacy cover, the pit was easily located in the high resolution CT scanner for a region of interest (RoI) CT scan (A1 to B1), thereby revealing a network of corroded boundaries surrounding the pit. This multiscale ‘scout and zoom’ approach combining different resolution X-ray CT scans has been reported previously, for example by Zhang et al<sup>21</sup>. However, to study these in detail destructive serial sectioning using a focused ion beam (FIB) was required. This relied on the careful registry of the sub-surface region of interest between the X-ray and FIB-SEM. This was achieved by relating the sub-surface corrosion sites of interest to the corresponding surface texture of the 3D X-ray image. This surface texture was then registered to the live image of the surface in the FIB-SEM (i.e. matching B2 to C1), thereby identifying where the FIB should be deployed to reveal the submerged features of interest in 3D (see overlay of sub-surface features in Fig. 1 B2 along with some of the main features which enable visualization of the correlation) by serial sectioning (C2) and electron back scattered diffraction (EBSD) imaging (C3). The final slice of the serially sectioned volume was

then extracted using the standard TEM sample preparation technique with a FIB<sup>22</sup>. This was first analysed in the scanning electron microscope using a novel transmission EBSD technique<sup>23,24</sup>. The slice was then transferred to a scanning transmission electron microscope (STEM) (D1) within which EDX was used to map the chemistry along and just ahead of the corrosion fronts of interest at the 10 nm scale (D2).

**Exemplar case study: Localized Corrosion in Austenitic Stainless Steel.** The pitting and intergranular corrosion of stainless steel have been widely researched as distinct mechanisms for material degradation<sup>25–27</sup>. Typically, pitting corrosion is observed in chloride-containing environments when exposed above the critical pitting temperature, resulting in sub-surface hemispherical or pear-shaped local attack, characteristically with a lacy cover that promotes the stability of pit growth<sup>28–30</sup>. In contrast, intergranular corrosion typically dominates when an environment corrodes susceptible grain boundaries, manifested as a regular corrosion front proceeding along grain boundaries with the consequent loss of grains often observed<sup>27,31</sup>. Here, correlative tomography has shown that in our case both act synergistically and in competition.

**Medium resolution X-ray CT: Following pit nucleation and growth.** Medium resolution X-ray CT allows the pitting of a significant region of a rod (2.5 mm diameter, ~5 mm height sample) to be observed non-invasively despite the associated lacy covers that prevent direct visual observation (see A1 and C1 of Fig. 1). Electrochemical polarization was employed to control the extent of pitting corrosion using an environmental cell in situ within the CT scanner. By repeatedly imaging the sample after discrete polarization cycles it

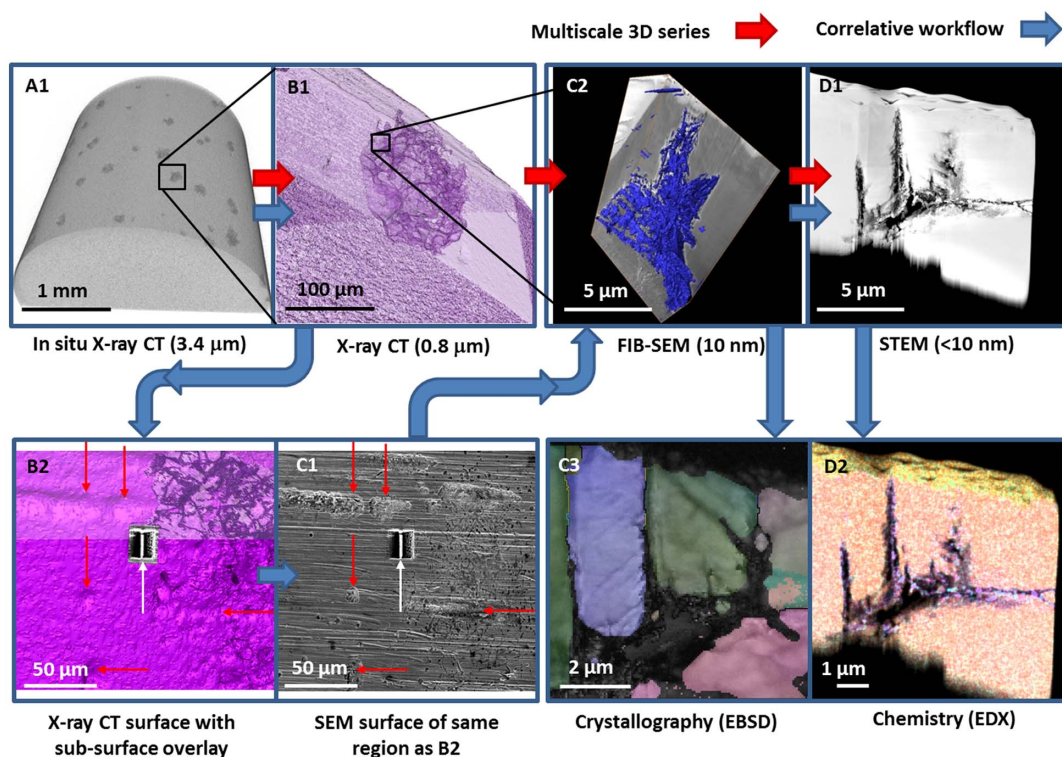


**Figure 1** | Correlative tomography workflow applied to study the nucleation and growth of pits in sensitized stainless steel linking together (A) medium and (B) high resolution X-ray CT with (C) serial sectioning FIB-SEM followed by EBSD imaging and (D) STEM-EDX imaging. B2 and C1 show the co-registry of surface texture as seen by X-ray CT and SEM imaging respectively with red arrows marking key features used in the correlation; B2 and C1 show the surface as viewed by X-ray CT and SEM respectively with the sub-surface extent of the intergranular corrosion displayed as a semi-transparent overlay on to the B2. C3 shows an EBSD map of the crystal orientation in Euler colours. D1 is a high angle annular dark image of the extracted slice and D2 presents STEM-EDX combining Fe, Ni, Cr, Mo, Si elemental maps. The magnifications and resolutions of the images collected by each instrument are indicated.



was possible to build up a time-lapse CT sequence of corrosion pit nucleation and growth. The first polarization cycle (scan 1) did not nucleate pitting corrosion, with the second cycle (scan 2), polarized to a higher electrochemical potential, a large number of discrete corrosion pits were formed. Although the lacy covers are not effectively observed at this resolution, the distribution of discrete pits can clearly be seen (A1 in Fig. 1) over a significant volume. Assuming a minimum size of 10 connected voxels (volumetric pixels) for a discrete pit, 76 pits were found to nucleate during the second polarization cycle over the monitored surface. The individual pit volumes (extracted from analysis of the 3D data) span more than four orders of magnitude with a maximum pit volume of  $7.5 \times 10^5 \mu\text{m}^3$ . This suggests that pits nucleated over a wide range of stable initiation potentials during the second polarisation cycle, if a diffusion controlled pit growth rate is assumed ( $t^{1/2}$  behaviour).

Interestingly, with the application of a third polarization cycle to a lower potential (equal in magnitude to the 1<sup>st</sup> cycle) at which no pits were previously observed to nucleate, the overall number of pits increased slightly to 84. New pits tended to have volumes in the range  $2\text{--}7 \times 10^2 \mu\text{m}^3$ , although one newly generated pit had a volume of  $130 \times 10^2 \mu\text{m}^3$  was also observed (most likely associated with crevice corrosion). More than 2/3 of the original 76 pits either kept their original size or grew by a negligible amount (<5% volume growth), and only around 1/4 of smaller pre-existing pits grew in volume by more than 10%. Whilst the first polarization cycle was insufficient to initiate corrosion these observations indicate that during the third polarization cycle (after corrosion had initiated during the second polarization cycle) the existing damage provided active pre-cursors for the growth of existing pits and also the nucleation of a few new pits. These newly formed pits may be the result of the presence of metastable pit nucleation sites, which were then re-activated during the third polarization cycle. Environmental conditions below the critical pitting potential are thus possibly able to activate pre-existing pit sites if the critical threshold was previously exceeded. While the sample scale is important in terms of developing a statistical understanding of the nucleation and growth process, medium resolution CT is not able to resolve any fine detail around individual pits. Consequently, increased resolution scans have been used to augment these observations.

**High resolution X-ray CT: Resolving competing mechanisms.** At the current time, X-ray CT cannot normally achieve a spatial resolution much better than  $1/1000^{\text{th}}$  of the sample size<sup>2</sup> unless region of interest (RoI) tomography is applied<sup>32</sup>. Here a RoI CT scan was applied to undertake high resolution ( $0.8 \mu\text{m}^3$  voxel size) imaging to study a single pit which was selected from the medium resolution image. The length of the 2.5 mm diameter rod was cut down so as to include the RoI to improve the X-ray transmission through the sample to increase the signal to noise and thus reduce the acquisition time. A virtual section of the pit taken from the resulting 3D image is shown in Fig. 2a). At this resolution the lacy cover evident in the SEM image (Fig. 1 C1 and Supplementary Fig. S2) can be clearly seen to remain virtually intact consistent with previous observations<sup>28,33</sup>. Several features are evident in the segmented 3D visualizations of the pit shown in Fig. 2 b) and c). At this scale it is evident that the hemispherical pit (red) is associated with a network of corroded boundaries (light blue). Their morphology is consistent with intergranular corrosion emanating from the pit. Surface breaching features are also highlighted (dark blue), which possibly stem from the pit growth process and go hand in hand with the formation of the perforated cover<sup>33</sup>; however though a contribution from intergranular corrosion penetrating the existing cover cannot be excluded. Indeed, subsequent higher resolution imaging of the surface above the pit by SEM (Fig. 1 C1 and Supplementary Fig. S2) showed many of the perforations to have narrow linear morphologies accompanied by light intergranular

attack indicating the presence of susceptible boundaries around the pit. In regions remote from the pit no intergranular attack was observed at the surface.

These observations suggest that the induced pitting corrosion leads to environmental conditions within the pit cavities (low pH and a high molarity of metal cations) that can cause the nucleation of intergranular corrosion from the pit walls. The sub-surface nucleation and progression of corrosion along grain boundaries is favoured above further growth of the pit volume itself, and the aggressive nature of the pit environment certainly provides the conditions for this scenario, with pit growth typically controlled by metal dissolution across a salt film present along the inner pit surface<sup>28,29</sup>. The nucleation of intergranular corrosion highlights that grain boundaries intersecting the pit can be preferentially attacked, providing rapid dissolution pathways in preference to general pit growth. However, it is not clear whether intergranular corrosion nucleated before, during or after the third polarization cycle, since the high-resolution scan was only conducted after the time-lapse medium resolution X-ray CT. The observed minimal growth in pit volumes may have been partly due to the intergranular corrosion emanating from within the pits (Fig. 2 and Supplementary Movie. S3) Interestingly, pit nucleation within pre-existing pits has been reported in the literature<sup>30</sup>; but this work appears to be the first report of intergranular corrosion nucleating within a pit, indicating how a change in the dominating corrosion mechanisms can occur.

**Serial sectioning FIB: exploring the crystallographic nature of the corrosion fronts.** Serial section FIB-SEM was directed towards a volume of interest (less than  $100 \mu\text{m}^3$ ) just beyond the pit periphery (Fig. 1 B2 and C1 and Supplementary Fig. S4) to study the corrosion network in more detail and to enable its crystallographic characterization. Using serial section FIB-SEM (50 nm thick slices,  $8.3 \text{ nm} \times 10.8 \text{ nm}$  pixel size), it was possible to image the corrosion front in 3D at a resolution of tens of nanometres (see Fig. 1 C2 and Fig 3a)). The corrosion front is composed of multiple fronts, some of which are connected to the sample surface. Thus, from the imaging, it appears that the corrosion fronts have grown beneath the surface from the pit with a morphology suggestive of grain boundary corrosion.

Furthermore transmission EBSD<sup>23,24</sup> orientation maps (in 2D or 3D) were acquired from the FIB prepared section<sup>22</sup>. The results from this novel transmission EBSD technique can be seen in the EBSD map shown in Fig 3b) three crystallographic sites for preferential corrosion can be readily differentiated: the high angle grain boundary (A) is most heavily attacked followed by coincidence site lattice (CSL) boundaries (B) and finally slip-bands (C). Interestingly, the CSL boundary is a  $\Sigma 11$  rather than the generally more common  $\Sigma 3$  twin and this has been identified from the misorientation of this boundary as measured from the EBSD orientation map. The  $\Sigma 11$  is more disordered than a  $\Sigma 3$  twin boundary and, hence, of a higher boundary energy. Consequently, the level of corrosion associated with the grain boundary, the CSL boundary and the slip band is consistent with their relative boundary surface energies with the grain boundary being the highest and the slip band the lowest with the surface energy of the CSL being intermediate.

The planes of these boundaries were also analysed from the 3D serial section FIB-SEM data. The CSL boundary plane (coincident with the (110) axis) could be traced through the FIB-SEM volume to the extracted slice and both were found to lie normal to the slice surface, indicating a low-energy coherent boundary interface structure (consistent with the geometrically straight, low-energy morphology i.e. lowest for an ideal  $\Sigma 11$  boundary) which would be expected to give increased corrosion resistance. Previously, a  $\Sigma 11$  grain boundary and boundary planes close to low index {hkl} planes have been found to be resistant to intergranular stress corrosion cracking<sup>34</sup>. However we have measured a deviation of up to 4 degrees from

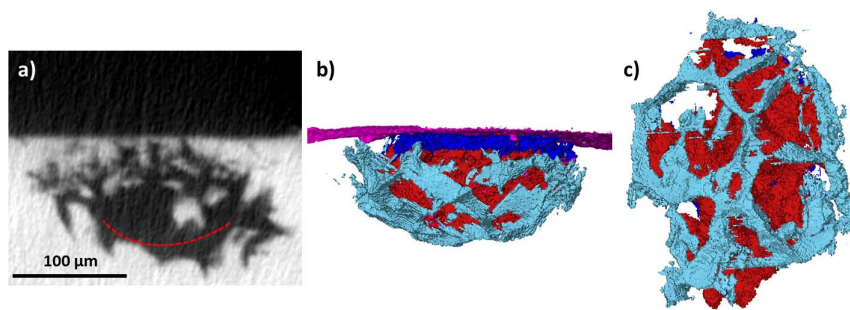


**Figure 2** | a) Virtual slice through the 3D image collected at high resolution (0.8  $\mu\text{m}$  voxel size) for the selected pit (approximate extent marked by red dashed line), b) side and c) underside 3D segmented visualization of the pit (red), local intergranular corrosion front network (light blue), surface perforations (dark blue) and sample surface (purple).

the ideal  $50.3^\circ$  misorientation (110) was measured along the  $\Sigma 11$  boundary (see Fig. 3b)), which is frequently associated with accommodated plastic strain and dislocations thus introducing additional energy and certain to increase the corrosion susceptibility of the  $\Sigma 11$  boundary. Corrosion has progressed along these boundaries, but to a far lesser extent when compared to the open, heavily corroded high angle grain boundary (A) in Fig. 3. Finally, EBSD cannot provide local chemistry information, which is known to be an important aspect controlling corrosion: thus chemically sensitive STEM-EDX is required.

**Chemically sensitive STEM: Capturing the chemistry around the corrosion front.** The last slice of the serially sectioned volume (D1 in Fig 1) was subsequently analysed using high resolution ( $<10$  nm pixel size) chemical imaging by means of STEM-EDX. Fig. 3d) clearly shows a Cr, Mo and Mn rich and Fe and Ni depleted corrosion product along the grain boundary (see also Supplementary Fig. S5). Ostensibly corrosion product can also be seen along the CSL boundary, although this is not clear along the slip band corrosion front. A closer look ahead of the corrosion front along the  $\Sigma 11$  boundary shows clear segregation of Cr and Mo, and a relative depletion of Fe and Ni with respect to the matrix

(Fig. 3e and Supplementary Fig. S6)), suggesting the effect of chemistry along with the structural disorder make this boundary a preferential corrosion path. Sensitization heat treatment can result in element segregation and the precipitation of second phase precipitates, with  $M_{23}C_6$ , sigma ( $\sigma$ ), chi ( $\chi$ ) and Laves phase ( $\eta$ ) all reported in grade 316 stainless steels<sup>35</sup>, but further work is required to definitively identify the Cr, Mo and Mn rich phases observed here. No such segregation was observed along the slip bands (Fig. 3f and Supplementary Fig. S7)), although these were not presented in an ideal orientation for analysis.

## Discussion

Correlative tomography has revealed the transition and competition between local corrosion mechanisms across multiple scales and in conjunction with co-registered crystallographic and chemical information. Medium resolution (3.4  $\mu\text{m}$ ) X-ray imaging allowed the proliferation and growth of pitting corrosion sites in sensitized austenitic stainless steel exposed to chloride-containing aqueous environment to be characterized despite their being concealed by perforated (lacy) covers. Higher resolution (0.8  $\mu\text{m}$ ) region of interest X-ray imaging of a typical pit uncovered a network of

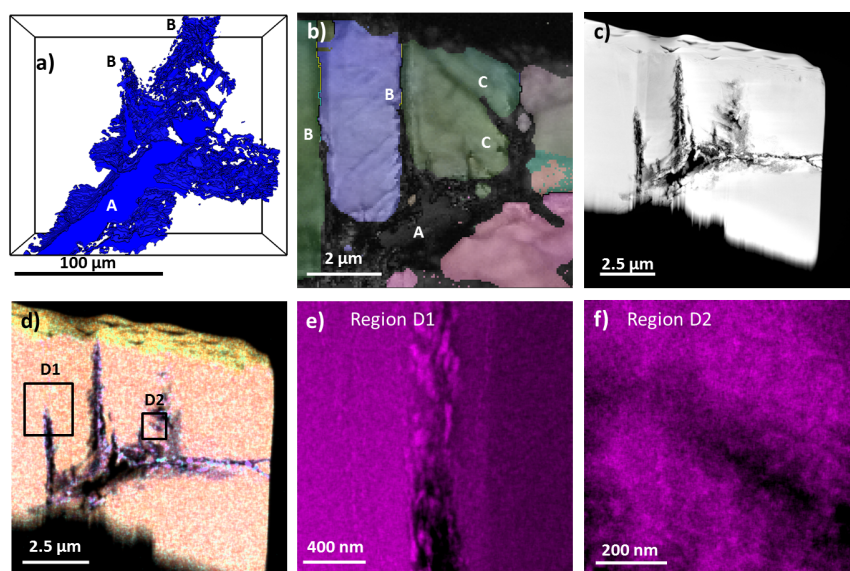


**Figure 3** | a) 3D visualization of a region of the crack front obtained by serial section FIB-SEM with the grain boundary (A) and CSL boundaries (B) indicated. b) EBSD map from final slice adjacent to the serial section FIB-SEM volume, showing crystal orientation Euler colours. (A) marks the grain boundary, (B) marks the CSL boundaries and (C) marks two examples of slip bands (referred to in main text). c) a high angle annular dark field (HAADF) image of the extracted slice, d) STEM-EDX image of the same slice showing a chemical map with a combination of Fe, Ni, Cr, Mo and Si. e) and f) high resolution elemental maps showing Cr distribution along and ahead of the corrosion front along e) the  $\Sigma 11$  boundary and f) the slip band are indicated in d) by D1 and D2 respectively.



intergranular corrosion surrounding the submerged pit some of which perforate the sample surface. 10 nm resolution serial sectioning using a focused ion beam has revealed 3D local corrosion morphologies. Electron backscatter diffraction (EBSD) of the final slice revealed the corrosion front proceeding along grain boundaries, coincidence site lattice (CSL) boundaries, as well as slip bands. The same slice was then analysed using scanning transmission electron microscopy-energy dispersive X-ray spectroscopy (STEM-EDX), local segregation of alloying elements have been found just ahead of the grain and CSL boundaries at the nanometre scale. Thus a combination of the chemical segregation and the boundary surface energies have defined the corrosion susceptibility, with the high angle grain boundaries being most susceptible followed by the CSL boundary and lastly the slip bands. This case study illustrates how the ability to co-register multifaceted/multiscale 3D information with the region of interest individually targeted at each sequential scale allows a unique understanding of the interaction of different corrosion mechanisms (see Supplementary Movie. S8).

More generally, correlative tomography provides access to a much larger range of scales for the same region than is possible by using one instrument alone. There are many cases where low resolution is required to survey large regions, for example to locate and image sparse features such as potentially critical defects, but for which structural information is required at much higher resolution, for example, to determine the exact nature of the crack tip propagation. This can be achieved over a very wide range of scales non-destructively by X-ray CT at multiple scales from micro (100–1  $\mu\text{m}$ ) to nano (1000–50 nm) resolution in tandem with serial section FIB-SEM or ultramicrotomy (>5 nm resolution) and even transmission electron tomography (>0.2 nm resolution). All are recorded for the same volume of interest and complemented with chemical and crystallographic information, as might be provided by 3D techniques such as 3D EBSD, 3D EDX and diffraction contrast tomography. Thus correlative tomography as presented here exploits in 3D all of the advantages offered by correlative microscopy in 2D i.e. helping to find a region of interest, providing multiscale context and combination of multimodal information<sup>1</sup>.

The rigorous linking of scales (whilst crucially being able to target the RoI at each successive scale) along with complementary information has widespread attractiveness from the study of biological systems through geological samples to materials science applications. Consequently, once automated 3D registration workflows have been established to seamlessly link together the different characterization techniques correlative tomography is likely to become as important a tool for the analysis of volumes of interest in 3D as correlative microscopy has become in 2D.

## Methods

A commercial grade 316H austenitic stainless steel sample in the solution annealed condition with a grain size of  $37 \pm 4 \mu\text{m}$  (excluding twin grain boundaries) was used for manufacturing cylindrical tensile sample, with a gauge length of 20 mm and gauge diameter of 2.5 mm. A sensitization heat-treatment at 650 °C for 24 hours in argon atmosphere was carried out to produce a microstructure susceptible to intergranular corrosion. The gauge was ground with SiC paper to a 2500 grit finish.

**Electrochemical corrosion testing** using time-lapse X-ray computer tomography (CT) was employed to follow the evolution of pitting corrosion in situ. A 25 mm (outer) diameter cylindrical Perspex tube was used as the environmental cell for the in-situ electrochemical experiments. The sample was centred in the environmental cell, connected to a potentiostat, and the set-up then mounted upon the rotation stage of the X-ray scanner. Electrochemical tests were carried out at room temperature using an IVIUM Compactstat and IivumSoft acquisition software. The sample acted as working electrode, with a platinum counter electrode, and a saturated Ag/AgCl miniature reference electrode. A 0.1 molar NaCl solution was used for all tests with the open circuit potential (OCP) recorded for 2 to 10 minutes until the potential was stable, followed by potentiodynamic polarization scans using a potential step-size of 1 mV/s.

**Time lapse medium resolution X-ray tomography** was undertaken at medium resolution (3.4  $\mu\text{m}$ ) in a lab-based Xradia Versa instrument using 150 kV X-ray energy at 4x optical magnification with an exposure time of 5 seconds and a total of 801 projections. Data were reconstructed using a Feldkamp-Davis-Kress (FDK)

reconstruction. A first assessment of the sample was carried out after polarization from  $-50 \text{ mV vs. OCP}$  to  $+350 \text{ mV}$ , but no pitting corrosion was observed in the CT data (scan 1). The second polarization step was conducted from  $-50 \text{ mV vs. OCP}$  to  $+580 \text{ mV}$  followed by an assessment using X-ray CT to see where corrosion had initiated (scan 2). A third CT scan was then carried out after polarizing the sample from  $-50 \text{ mV vs. OCP}$  to  $+350 \text{ mV}$ , using a step size of  $4 \text{ mVs}^{-1}$  (scan 3). After each potentiodynamic polarization, the tensile sample was disconnected from the potentiostat to allow unconstrained rotations for CT assessment but with the sample remaining in situ in the NaCl solution the whole time. Each CT experiment scan was conducted using the same imaging conditions.

**High resolution X-ray CT.** After the corrosion experiments, high resolution X-ray CT scanning was also conducted on an Xradia Versa X-ray microscope on a 1.5 mm thick diametral slice from the original 2.5 mm diameter volume capturing the corrosion pit of interest. From this volume it was possible to achieve high resolution (0.8  $\mu\text{m}^3$  voxel size) resolution using region of interest imaging with superior contrast compared the overview scan of the entire sample, which was limited by both the field of view and the thickness of the steel. The imaging conditions used were 140 kV at 4x optical magnification with an exposure time of 15 seconds per projection and a total of 3201 projections. Data were reconstructed using an FDK reconstruction.

**Serial section FIB-SEM:** was conducted on a FEI Nova Nanolab Dual Beam microscope using the automated Slice and View™ software utilizing both the electron and gallium ion beams, with detection via secondary electrons using the Everhart-Thornley detector (ETD) at 5 kV accelerating voltage and 1 nA beam current. A standard procedure for the creation of the cross sections was followed once the RoI had been identified. Side trenches were also excavated to alleviate re-deposition build up. The serial sections of nominal 50 nm thickness were prepared with the FIB using 1 nA current at 30 kV. The imaging pixel size was 87 nm<sup>2</sup>. A total of 60 slices were recorded taking ~8 hours. For an overview of working with the FIB for specimen preparation and serial sectioning please see e.g.<sup>36,37</sup> and references therein.

**Crystallographic and Chemical analysis.** Using the same FEI Nova Nanolab FIB-SEM a TEM lamella sample was prepared adjacent to the final slice of the Slice and View™ volume and extracted in situ using an Omniprobe micromanipulator. The lamella was then attached to a copper TEM grid and welded in place by depositing Pt at the interface. This sample was first analysed using transmission EBSD analysis using 30 kV accelerating voltage, 3.2 nA probe current and 2 mm working distance with a 50 nm step size. The data were gathered using the Oxford Instruments NordlysNano detector and AZtecHKL software version 2.0.

STEM and EDX spectrum imaging were performed using a probe-side aberration-corrected FEI Titan G2 80–200 S/TEM operated at 200 kV. STEM images were collected using a convergence angle of 18 mrad and a high angle annular dark-field (HAADF) detector with an inner angle of 55 mrad. EDX compositional analysis was performed using the Super-X detector configuration ( $4 \times 30 \text{ mm}^2$  SDDs) with a solid angle of  $\sim 0.7 \text{ srad}$  and a beam current of  $\sim 0.6 \text{ nA}$ . Spectrum images were acquired with non-standard times, until total counts were deemed sufficient, with a dwell time of 30  $\mu\text{s}$  per pixel. For display purposes, all spectrum images were processed using a 3-pixel smoothing window in the Bruker Esprit software.

**3D visualization.** All of the reconstructed data were analysed and visualized in 3D using FEI Avizo software.

1. Caplan, J., Nihammer, M., Taylor, R. M. & Czymbek, K. J. The power of correlative microscopy: multi-modal, multi-scale, multi-dimensional. *Curr. Op. Struc. Biol.* **21**, 686–69 (2011).
2. Maire, E. & Withers, P. J. Quantitative X-ray Tomography. *Int. Mater. Rev.* **59**, 1–43 (2014).
3. Stock, S. R. *MicroComputed Tomography: Methodology and Applications*, (CRC Press, Boca Raton, FL, USA, 2009).
4. Herbig, M. *et al.* 3-D growth of a short fatigue crack within a polycrystalline microstructure studied using combined diffraction and phase-contrast X-ray tomography. *Acta Mat.* **59**, 590–601 (2011).
5. Shearing, P. R., Gelb, J. & Brandon, N. P. X-ray nano computerised tomography of SOFC electrodes using a focused ion beam sample-preparation technique. *J. Eur. Ceram. Soc.* **30**, 1809–1814 (2010).
6. Turnbull, A., Wright, L. & Crocker, L. New insight into the pit-to-crack transition from finite element analysis of the stress and strain distribution around a corrosion pit. *Corr. Sci.* **52**, 1492–1498 (2010).
7. Kinahan, P. E., Hasegawa, B. H. & Beyer, T. X-Ray-Based Attenuation Correction for Positron Emission Tomography/Computed Tomography Scanners. *Sem. Nuc. Med.* **33**, 166–179 (2003).
8. Thompson, G. E. *et al.* Revealing the three dimensional internal structure of aluminium alloys. *Surf. Interf. Anal.* **45**, 1536–1542 (2013).
9. Gupta, C. *et al.* Study of creep cavitation behavior in tempered martensitic steel using synchrotron micro-tomography and serial sectioning techniques. *Mat. Sci. Eng. A* **564**, 525–538 (2013).
10. Handschuh, S., Baeumler, N., Schwaha, T. & Ruthensteiner, B. A correlative approach for combining microCT, light and transmission electron microscopy in a single 3D scenario. *Front. Zoo.* **10**, 44 (2013).



11. Tariq, F., Haswell, R., Lee, P. D. & McComb, D. W. Characterization of hierarchical pore structures in ceramics using multiscale tomography. *Acta Mat.* **59**, 2109–2120 (2011).
12. Chen, B. *et al.* Three-Dimensional Structure Analysis and Percolation Properties of a Barrier Marine Coating. *Sci. Rep.* **3**, 1177 (2013).
13. Withers, P. J. *et al.* 3-D Materials Characterization Over a Range of Time and Length Scales. *Adv. Mater. Processes* **170**, 28–32 (2012).
14. Sok, R., Varslot, T. & Ghous, A. *et al.* Pore scale characterization of carbonates at multiple scales: integration of micro-CT BSEM and FIBSEM. *Petrophys.* **51**, 379–387 (2010).
15. Bera, B., Mitra, S. K. & Vick, D. Understanding the micro structure of Berea Sandstone by the simultaneous use of micro-computed tomography (micro-CT) and focused ion beam-scanning electron microscopy (FIB-SEM). *Micron* **42**, 412–418 (2011).
16. Sengle, G., Tufa, S. F., Sakai, L. Y., Zulliger, M. A. & Keene, D. R. A Correlative Method for Imaging Identical Regions of Samples by Micro-CT, Light Microscopy, and Electron Microscopy: Imaging Adipose Tissue in a Model System. *J. Histochem Cytochem* **61**, 263 (2013).
17. Zehbe, R., Riesemeier, H., Kirkpatrick, C. J. & Brochhausen, C. Imaging of articular cartilage – Data matching using X-ray tomography, SEM, FIB slicing and conventional histology. *Micron* **43**, 1060–1067 (2012).
18. Gatz, A. S., Beck, F., Rigort, A., Baumeister, W. & Plitzko, J. M. Correlative microscopy: Bridging the gap between fluorescence light microscopy and cryo-electron tomography. *J. Struc. Biol.* **160**, 135–145 (2007).
19. Marrow, T. J. *et al.* Three dimensional observations and modelling of intergranular stress corrosion cracking in austenitic stainless steel. *J. Nuc. Mat.* **352**, 62–74 (2006).
20. van Driel, L. F., Valentijn, J. A., Valentijn, K. M., Koning, R. I. & Koster, A. J. Tools for correlative cryo-fluorescence microscopy and cryo-electron tomography applied to whole mitochondria in human endothelial cells. *Eur. J. Cell Biol.* **88**, 669–684 (2009).
21. Zhang, T., Maire, E., Adrien, J., Onck, P. R. & Salvo L. Local Tomography Study of the Fracture of an ERG Metal Foam. *Adv. Eng. Mater.* **15**, 767–772 (2013).
22. Giannuzzi, L. A. & Stevie, F. A. A review of focused ion beam milling techniques for TEM specimen preparation. *Micron* **30**, 197–204 (1999).
23. Keller, R. R. & Geiss, R. H. Transmission EBSD from 10 nm domains in a scanning electron microscope. *J. Micros.* **245**, 245–251 (2012).
24. Trimby, P. W. Orientation mapping of nanostructured materials using transmission Kikuchi diffraction in the scanning electron microscope. *Ultramicros.* **120**, 16–24 (2012).
25. Newman, R. C. 2001 W.R. Whitney Award Lecture: Understanding the Corrosion of Stainless Steel. *Corrosion* **57**, 1030–41 (2001).
26. Ghahari, S. M. *et al.* In situ synchrotron X-ray micro-tomography study of pitting corrosion in stainless steel. *Corr. Sci.* **53**, 2684–7 (2011).
27. Engelberg, D. L. [Chapter 2.08 Intergranular Corrosion] *Shreir's Corrosion*, [Cottis, B., Graham, M., Lindsay, R., Lyon, S., Richardson, T., Scantlebury, D. *et al.* (Ed.s)] [810–27] (Elsevier, Oxford, 2010).
28. Ernst, P. & Newman, R. C. Pit growth studies in stainless steel foils. I. Introduction and pit growth kinetics. *Corr. Sci.* **44**, 927–41 (2002).
29. Ernst, P. & Newman, R. C. Pit growth studies in stainless steel foils. II. Effect of temperature, chloride concentration and sulphate addition. *Corr. Sci.* **44**, 943–54 (2002).
30. Ernst, P. & Newman, R. C. Explanation of the effect of high chloride concentration on the critical pitting temperature of stainless steel. *Corr. Sci.* **49**, 3705–15 (2007).
31. Cihal, V. *Intergranular Corrosion of Steels and Alloys Elsevier* (1984)
32. Kyrieleis, A., Titarenko, V., Ibison, M., Connelly, T. & Withers, P. J. Region-of-interest tomography using filtered back projection: assessing the practical limits. *J. Micros.* **241**, 69–82 (2011).
33. Ernst, P., Laycock, N. J., Moayed, M. H. & Newman, R. C. The mechanism of lacy cover formation in pitting. *Corr. Sci.* **39**, 1133–6 (1997).
34. King, A., Johnson, G., Engelberg, D. L., Marrow, T. J. & Ludwig, W. Observation of Intergranular Stress Corrosion Cracking in a Grain-Mapped Polycrystal. *Science* **321**, 382–5 (2008).
35. Lai, J. K. L. A review of precipitation behaviour in AISI type 316H stainless steel. *Mater. Sci. Eng.* **61**, 101–109 (1983).
36. Volkert, C. A. & Minor, A. M. Focussed Ion beam microscopy and micromachining. *MRS Bull.* **32**, 389–399 (2007).
37. Groeber, M. A., Haley, B. K., Uchic, M. D., Dimiduk, D. M. & Ghosh, S. 3D reconstruction and characterization of polycrystalline microstructures using a FIB-SEM system. *Mater. Char.* **57**, 259–273 (2006).

## Acknowledgments

Our gratitude and thanks to the following individuals: Carmen van Vilsteren (FEI) for helpful comments and guidance, Ellen Williams (BP) for much of the inspiration behind this work and general comments and help from Pascal Doux (FEI), Daniel Lichau (FEI) and Rob Bradley (MXIF, University of Manchester). We gratefully acknowledge BP funding and encouragement as well as experimental support from FEI, and Zeiss Xradia. Funding from FEI for TLB to work at the University of Manchester is gratefully acknowledged. CO acknowledges EPSRC (EP/I036397/1) and NDA (NPO004411A-EPS02) for financial support. The X-ray CT experiments were undertaken within the MXIF at the University of Manchester, established with funding from EPSRC through grants EP/F007906, EP/I02249X and EP/F028431. Funding for the FEI Titan G2 80-200 S/TEM was provided by HM Government (UK) in association with research capability of the Nuclear Advanced Manufacturing Research Centre.

## Author Contributions

T.L.B and P.J.W. envisioned the original correlative tomography concept. T.L.B., D.L.E., G.E.T. and P.J.W. wrote the paper and made the discussion of the results. T.L.B. and P.J.W. created the figures. S.A.M. and T.L.B. recorded and analysed the X-ray tomography results. A.G. recorded the FIB-SEM and EBSD results. A.G. and T.L.B. analysed the EBSD and FIB-SEM results. T.L.B., R.G., M.J. G.E.T. and P.J.W. designed, prepared and executed the correlation between tools. T.S., S.J.H., and T.L.B. recorded and analysed the TEM results. C.O., F.A. and D.L.E. designed, executed and analysed the corrosion tests.

## Additional information

**Supplementary information** accompanies this paper at <http://www.nature.com/scientificreports>

**Competing financial interests:** The authors declare no competing financial interests.

**How to cite this article:** Burnett, T.L. *et al.* Correlative Tomography. *Sci. Rep.* **4**, 4711; DOI:10.1038/srep04711 (2014).



This work is licensed under a Creative Commons Attribution-NonCommercial-ShareAlike 3.0 Unported License. The images in this article are included in the article's Creative Commons license, unless indicated otherwise in the image credit; if the image is not included under the Creative Commons license, users will need to obtain permission from the license holder in order to reproduce the image. To view a copy of this license, visit <http://creativecommons.org/licenses/by-nc-sa/3.0/>